Digital Discovery

ROYAL SOCIETY OF CHEMISTRY

PAPER

View Article Online
View Journal | View Issue

Cite this: *Digital Discovery*, 2024, **3**, 173

Automatic mechanism generation involving kinetics of surface reactions with bidentate adsorbates†

Bjarne Kreitz, ‡*[a] Katrín Blöndal,‡[a] Kirk Badger,[a] Richard H. West [b] and C. Franklin Goldsmith *[a]

Received 15th September 2023
Accepted 5th December 2023

DOI: 10.1039/d3dd00184a

rsc.li/digitaldiscovery

The open-source Reaction Mechanism Generator (RMG) has been enhanced with new features to handle multidentate adsorbates. New reaction families have been added based upon *ab initio* data from 26 reactions involving $C_xO_yH_z$ bidentate adsorbates with two heavy atoms on Pt(111). Additionally, the estimation routines for thermophysical properties were improved and extended towards bidentate species. Non-oxidative dehydrogenation of ethane over Pt(111) is used as a case study to demonstrate the effectiveness of these new features. RMG not only discovered the pathways from prior literature but also uncovered new elementary steps involving abstraction reactions. Various mono- and bimetallic catalysts for this process were screened using linear scaling relations within RMG, where a unique mechanism is generated for each catalyst. These results are consistent with prior literature trends, but they add additional insight into the rate-determining steps across the periodic table. With these additions, RMG can now explore more intricate reaction mechanisms of heterogeneously catalyzed processes for the conversion of larger molecules, which will be particularly important in fuel synthesis.

Introduction

The elucidation of reaction mechanisms on transition metal surfaces is the first step in the construction of microkinetic models for heterogeneously catalyzed reactions. This process is often performed on an *ab initio* basis using density functional theory (DFT) calculations. First-principles-based microkinetic models can be used to tailor catalytic materials and, when combined with multiscale models, can enhance reactor design and performance.[1,2] With the advancement in computational power, investigating mechanisms for the conversion of larger molecules is now a common task. For example, Zijlstra *et al.*[3] created a microkinetic model for the Fischer–Tropsch synthesis with a first-principles-based description of the C_3 chemistry. Microkinetic models for the conversion of these large molecules necessarily involve highly unsaturated hydrocarbon adsorbates with multiple heavy atoms (here defined to be any element larger than hydrogen). When these large, unsaturated molecules adsorb, they can form multiple covalent bonds with the surface to form a stable, closed shell adsorbate. Species that bind to the surface through more than one atom are referred to as multidentate/polydentate adsorbates. Practically any reaction mechanism that involves adsorbates with two or more heavy atoms can contain multidentate species.

Additionally, processes with large molecules encompass extensive reaction networks with numerous possible intermediates and elementary steps. Constructing the reaction mechanisms manually requires considerable chemical knowledge to compile an extensive list of possible elementary steps in the vast reaction space. Software tools are available to help with this task by compiling lists of elementary steps from an initial pool of species.[4–6] However, it remains the researcher's responsibility (and challenge) to identify the kinetically relevant pathways with DFT calculations or (first-principles-based) estimation routines. Due to the high computational cost associated with electronic structure calculations for heterogeneous systems and limited computational resources, some chemical pathways remain unexplored. Thus, the determination of kinetic pathways is subject to bias. The Reaction Mechanism Generator (RMG)[7–9] creates microkinetic models automatically containing only kinetically relevant pathways using a rate-based algorithm, while probing the entire chemical reaction space of a system. This selection is achieved through an on-the-fly parameterization of all possible elementary steps and intermediates based on *ab initio* databases and estimation routines.

RMG is a well-established tool to construct gas-phase mechanisms for complex systems, *e.g.*, the pyrolysis of jet

[a]*School of Engineering, Brown University, Providence, RI 02912, USA. E-mail: bjarne_kreitz@brown.edu; franklin_goldsmith@brown.edu*

[b]*Department of Chemical Engineering, Northeastern University, Boston, MA 02115, USA*

† Electronic supplementary information (ESI) available: Transition state theory and BEP relation equations, enthalpy of reaction comparison, potential energy diagrams, electronic structure calculations results. See DOI: https://doi.org/10.1039/d3dd00184a

‡ These authors contributed equally to this work.

fuel.[10] Functionalities for heterogeneous catalysts, in contrast, have been added relatively recently.[11] Previous studies on the catalysis branch of RMG have focused on expanding the thermophysical adsorbate database,[12,13] improving kinetics databases and rate rules of surface reaction families,[13,14] and developing important features such as linear scaling relations.[15] With these advancements, RMG has successfully generated microkinetic models for the CO_2 methanation on Ni(111)[14,16,17] and the oxidation of light hydrocarbons.[12,13,15] It was also possible to include rigorous quantification of correlated uncertainties in the generation procedure.[14,17,18] However, these studies have primarily focused on the chemistry of small molecules. Although RMG was able to construct mechanisms involving larger hydrocarbons, the reliability of its predictions for the C_2 chemistry and beyond have not yet been thoroughly explored. One of the reasons for the limitations of RMG in dealing with larger molecules is its lack of functionalities for multidentate adsorbates, which was only previously achieved by providing precompiled reaction libraries.[13] This limitation can cause the software to miss pathways that involve multidentate surface species, which are crucial in many important catalytic processes.

Bidentate species are central to the reaction mechanism for the dehydrogenation of light alkanes, which is becoming increasingly important to convert large amounts of shale gas to valuable alkenes.[19] The dehydrogenation of light alkanes can happen under either oxidative or non-oxidative conditions.[19–21] Although the oxidative route is energetically favorable, it requires O_2 and produces H_2O as a byproduct; non-oxidative dehydrogenation (NDH), in contrast, leads to valuable H_2 as a side product.[21] The endothermic NDH is carried out over Pt or CrO_x-based catalysts at temperatures of 500 to 600 °C.[22–24] A common problem for dehydrogenation is the identification of catalysts that can achieve a high alkane conversion while maintaining a high selectivity towards alkenes and high resistance to coke formation. The desired features can be obtained by alloying Pt or Pd with a range of other transition metals.[19,25–27] A promising candidate that is used already at the industrial scale is Pt_3Sn.[28]

Expanding the features of RMG to accommodate multidentate species is necessary to explore the complex dehydrogenation chemistry over the intricate active site motifs and aid in the elucidation of the reaction mechanism. In this study, we present new functionalities for multidentate adsorbates that enhance RMG's ability to explore reaction mechanisms for the conversion of larger molecules. These updates require (i) improved estimation routines for the thermophysical properties of multidentate species and (ii) new reaction families with accurate rate rules. We performed *ab initio* calculations for 26 reactions involving H/C/O-containing bidentate species on Pt(111) to create Brønsted(Bell)–Evans–Polanyi (BEP) relations for the new families. The updated software is then applied to investigate the NDH of ethane over Pt(111) as a representative test case for larger molecules. Further, we use linear scaling relations to screen across the periodic table, including bimetallic alloys, to demonstrate RMG's capabilities in identifying more active and selective catalysts. The significant updates to RMG greatly improve the exploration of all possible pathways of a mechanism, facilitating the automated discovery of more intricate reaction systems.

Methods

Electronic structure theory

DFT calculations were performed with the plane-wave code Quantum ESPRESSO[29,30] using the vdW-DF-cx functional.[31,32] SG15 Optimized Norm-Conserving Vanderbilt (ONCV) pseudopotentials, generated with the ONCVPSP code,[33,34] were used. The optimized lattice constant with the vdW-DF-cx functional was found to be 3.93 Å for Pt in good agreement with the experimental value. The adsorbate-Pt(111) systems were modeled using a 4-layer Pt(111) slab with a 3×3 unit cell and 17 Å of vacuum between the top of the slab and the bottom of the repeated image. A step-wise approach was employed in the geometry optimizations. In the first step, the adsorbates were relaxed on the surface with all atoms fixed in their bulk geometry. In the second step, the bottom two layers of the surface atoms were held fixed, while the top two layers were relaxed with the adsorbates. A plane-wave cutoff of 50 Ry and $(5 \times 5 \times 1)$ *k*-point grid was used for both steps and the Marzari–Vanderbilt smearing method[35] with a smearing width of 0.02 Ry. The LBFGS algorithm in the Atomic Simulation Environment (ASE)[36] was used for geometry relaxations with a maximum force convergence criterion of 0.025 eV $Å^{-1}$. Sella, an open-source saddle point optimizer,[37] was used to find the transition states with a maximum force convergence criterion of 0.05 eV $Å^{-1}$. In most cases, a robust constrained force interpolation method[38] was used to obtain the initial guesses for Sella. Vibrational frequencies of the adsorbates were calculated *via* finite differences in ASE. A higher plane-wave cutoff of 60 Ry and a $(5 \times 5 \times 1)$ *k*-point grid was used for the single-point energy calculations.

New features in RMG for multidentate adsorbates

RMG version 3.0 (ref. 9) and its functionalities are described in greater detail in ref. 7, 8 and 39. Ref. 11 describes special features for generating mechanisms for heterogeneously catalyzed reactions. In this paper, we focus only on the parts that were updated: the database of thermophysical properties and the reaction families, including their kinetic estimation routines. This update is focused primarily on H/C/O-containing adsorbates; similar expansion for nitrogen functionality will be the subject of future work.

Adsorption correction database. When RMG encounters a species that is not present in the adsorbate thermochemistry database, it needs to estimate the thermophysical properties. To do so, RMG first desorbs the species and determines the properties of the gas-phase precursor – either from a precompiled database, or *via* Benson's group additivity. The thermophysical properties of the gas-phase precursor X_{gas} (where X is the enthalpy of formation $\Delta_f H$ (298 K), entropy S (298 K), and heat capacity $c_p(T)$) are then corrected through an adsorption correction $\Delta X_{adsorption}$ to account for the heat of adsorption, the

loss of translational/rotational degrees of freedom upon adsorption, and the gain of new surface vibrational modes.[11,40]

$$X_{\text{adsorbate}} = X_{\text{gas}} + \Delta X_{\text{adsorption}} \quad (1)$$

The adsorption corrections are based on adsorbates in the Pt(111) database, which are organized in a hierarchical tree, with the most generic nodes at the top level and more specific child nodes. RMG replaces functional groups of the discovered adsorbate with wildcards R to find a suitable adsorption correction, and descends the tree to the most specific node that has data.

Previously, the corrections were created based on the thermochemistry database of adsorbates with no more than two heavy atoms on Pt(111).[12] Since the publication of the RMG database paper,[12] the Pt database has been extended to include 113 adsorbates containing many multidentate species,[13,18] whereas the adsorption correction database remained unchanged. In the present work, we overhaul the adsorption correction tree for monodentate and bidentate species by providing new child nodes to provide more accurate thermophysical estimates for unknown species, especially for bidentate adsorbates. The adsorption corrections for every node are an average of all species or underlying child nodes at the higher levels. Fig. 1 shows the adsorption correction tree for bidentate adsorbates. Additionally, we created new trees for bidentate adsorbates with bridging atoms between the two adatoms and tridentate species.

Reaction families. The kinetics database in RMG consists of reaction templates with bond-breaking or forming recipes grouped into reaction families, *e.g.*, dissociation of single bonds. The chemical reaction space is explored during the mechanism generation by applying all suitable reaction templates to the chemical graphs of the reactants. Thus, all possible elementary steps are considered within the space spanned by the available reaction templates. Each family has a set of training reactions to accompany it and estimation routines organized in a hierarchical database. The tree-structured database has general estimation rules for the top-level nodes and more specific rules for the children nodes, which provide a more accurate estimate of the reaction kinetics. Estimation rules are either based on BEP relations or automatically generated from the training reactions. The automated tree generation is described in detail in ref. 39. During mechanism generation, RMG first searches a reaction library or a higher-priority seed mechanism for a direct match. If no match is found, RMG will use the tree-structured estimation routines and climb down the tree to the most specific node with a BEP or an automatically generated rule based on the training reactions to determine the kinetics. The highest accuracy is obtained if the reaction is a direct match, and the more generalized rate rules lead to higher uncertainties. In this work, we use only a reaction library combined with BEP estimation rules for the reaction families, as described below.

Five new reaction families were created to extend the capabilities of RMG to bidentate or multidentate adsorbates, which are shown in Table 1. We refer to them in a manner consistent with their names in the RMG database. Surface_Bidentate_-Dissociation is a template to dissociate a bidentate adsorbate with a single bond into two monodentate species. A monodentate adsorbate can undergo bond scission from an R group to form a bidentate and a monodentate adsorbate, which is described with the Surface_Dissociation_to_Bidentate template. Physisorbed species with double or triple bonds can form bidentate adsorbates (Surface_Adsorption_Bidentate). A similar reaction can occur for monodentate species (Surface_-Monodentate_to_Bidentate), where the species bends over to form an additional bond with the surface. Surface_Adsorption_Bidentate provides a recipe for the direct adsorption of a gas-phase molecule as a bidentate species, such as C_2H_4. Additionally, training data was generated for the dissociation of a bidentate species, where the product remains a bidentate. This bond-breaking recipe is grouped in the (Surface_Dissociation) family, which was introduced in the original development of RMG-Cat.[11] Templates for the (Surface_Dissociation) family may not always involve a bidentate adsorbate.

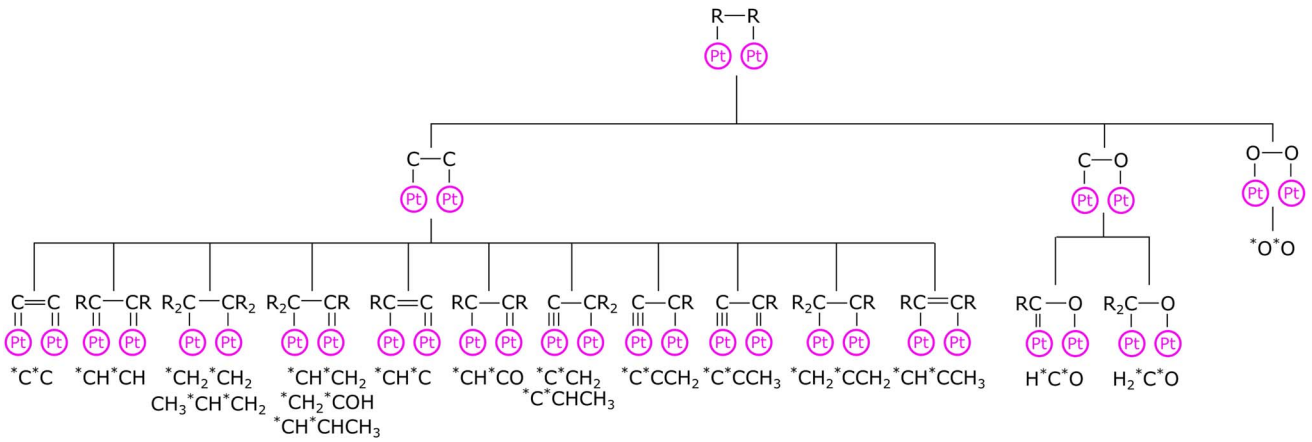

Fig. 1 Adsorption correction tree for bidentate adsorbates. R denotes a wildcard that can be replaced by any functional group. All adsorbates that are used to train a child node are listed below the node.

Table 1 New and updated reaction families in RMG to provide functionalities for bidentate adsorbates

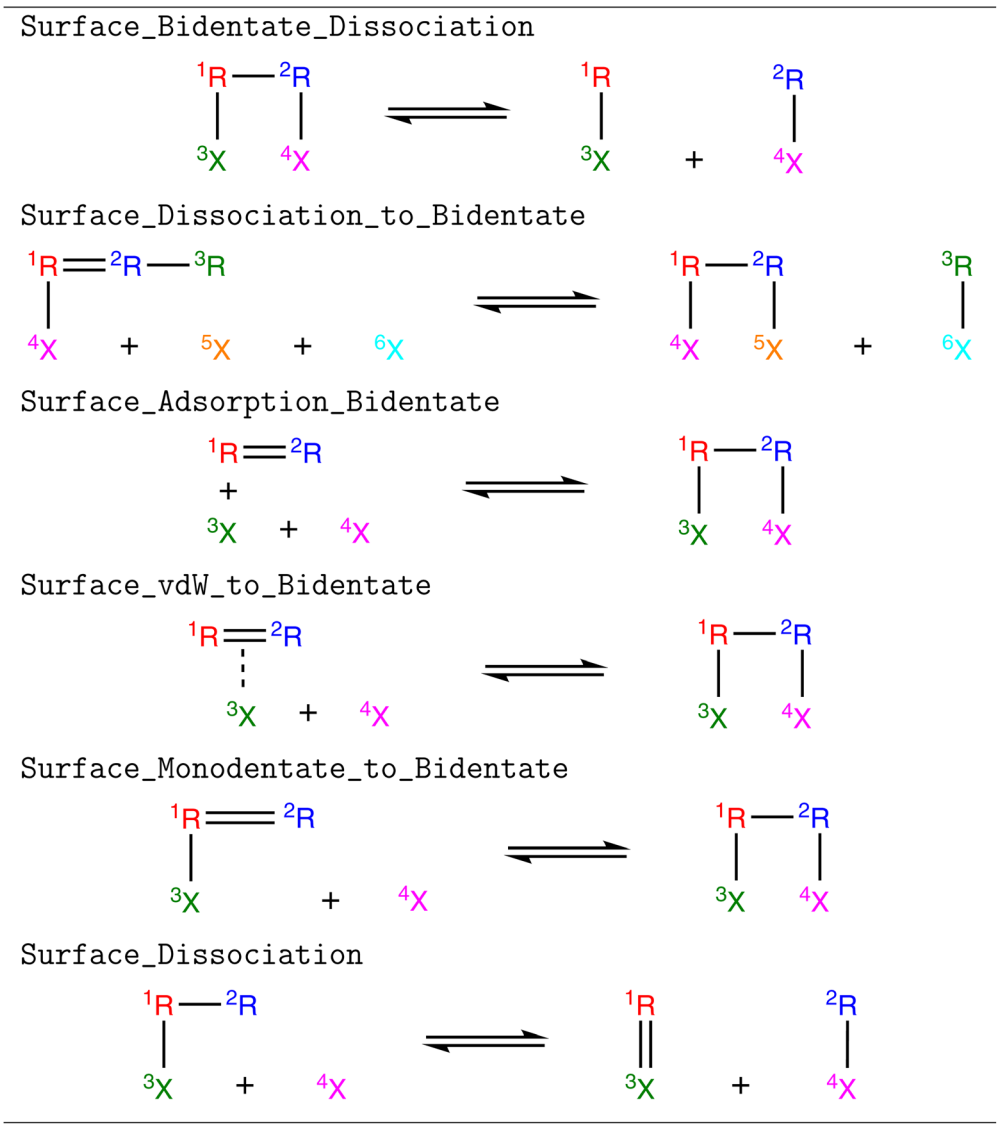

Results and discussion

The DFT results for the energy barriers and reaction enthalpies for a set of 26 unique reactions belonging to the six considered reaction families are listed in Table 2. Raw DFT energies and vibrational modes for these reactions are provided in the ESI.† All data and scripts are made publicly available in ref. 41. Detailed potential energy diagrams for the reactions in the Surface_Bidentate_Dissociation, Surface_Dissociation, and Surface_Dissociation_to_Bidentate families are shown in the ESI in Fig. S1–S3,† respectively. The rate constants for the reactions with a well-defined energy barrier were computed assuming fixed (harmonic) transition state theory over a temperature range of 300 to 2000 K. The partition functions of the transition state $Q^{\ddagger}$ and initial state Q_R, as well as the subsequent rate constants k_{TST} in the low-coverage limit, are calculated with in-house Python routines.

$$k_{TST}(T) = \frac{k_B T}{h} \frac{Q^{\ddagger}(T)}{Q_R(T)} e^{\left(-\frac{\Delta E_0}{k_B T}\right)} \quad (2)$$

For consistency with the convention in RMG of defining the exothermic direction as the forward direction, rate constants for reactions 1d–1g and 3c were calculated in the exothermic direction and the fitted Arrhenius parameters for them were used in the RMG training reactions database. Two of the Surface_vdW_to_Bidentate reactions, 4a and 4c, all the Surface_Adsorption_Bidentate reactions (5a, 5b and 5c), and reactions 6a and 6c of the Surface_Monodentate_to_Bidentate were found to have no potential energy barrier. Therefore, fixed transition-state theory could not be used to calculate the rate constants; a more rigorous variational analysis would be necessary. As an approximate solution, Arrhenius expressions with a pre-exponential factor of 10^{21} cm^2 mol^{-1} s^{-1} and E_a =

Table 2 The reaction labels given to the list of reactions considered, the DFT energy barrier ΔE_0, the heat of reaction ΔH_{rxn} considering the most stable final state. For reactions where "–" appears in the ΔE_0 column, no energy barrier was found

No		ΔE_0 (kJ mol^{-1})	ΔH_{rxn} (kJ mol^{-1})	A (cm^2 mol^{-1} s^{-1}) or A (cm^4 mol^{-2} s^{-1})† or A (s^{-1})‡ or A (1)¶	E_a (kJ mol^{-1})
Surface_Bidentate_Dissociation					
1a	*C*C ⇌ *C + *C	103	−77	$4.22 \times 10^{12\ddagger}$	104
1b	*CH*C ⇌ *CH + *C	78	−80	$1.30 \times 10^{12\ddagger}$	77
1c	*CH*CH ⇌ *CH + *CH	88	−49	$7.93 \times 10^{12\ddagger}$	90
1d	*CH*CH$_2$ ⇌ *CH + *CH$_2$	135	0	$2.74 \times 10^{13\ddagger}$	140
1e[a]	*CH$_2$*CH$_2$ ⇌ *CH$_2$ + *CH$_2$	218	71	$2.61 \times 10^{15\ddagger}$	227
1f[a]	*CH*O ⇌ *CH + *O	180	40	$6.50 \times 10^{12\ddagger}$	183
1g[a]	*CH$_2$*O ⇌ *CH$_2$ + *O	141	30	$3.61 \times 10^{13\ddagger}$	145
Surface_Dissociation					
2a	*CH*CH$_2$ + * ⇌ *CH*CH + *H	68	−7	9.5×10^{21}	72
2b	*CH$_2$*CH$_2$ + * ⇌ *CH$_2$*CH + *H	55	−6	4.45×10^{21}	59
2c	*CH$_2$*O + * ⇌ *CH*O + *H	1	−74	1.75×10^{21}	2
2d[a]	*C*CH$_2$ + * ⇌ *C*CH + *H	128	93	2.81×10^{22}	134
2e[a]	*CH*CH + * ⇌ *C*CH + *H	130	70	2.84×10^{22}	137
2f	*CH*CH$_2$ + * ⇌ *C*CH$_2$ + *H	44	−17	9.69×10^{21}	48
Surface_Dissociation_to_Bidentate					
3a	*CH$_2$CH$_3$ + 2* ⇌ *CH$_2$*CH$_2$ + *H	42	−41	$1.67 \times 10^{30\dagger}$	46
3b	*CHCH$_3$ + 2* ⇌ *CH*CH$_2$ + *H	45	−34	$1.95 \times 10^{30\dagger}$	49
3c[a]	*CH$_2$OH + 2* ⇌ *CH$_2$*O + *H	50	1	$2.47 \times 10^{29\dagger}$	52
3d[a]	*CCH$_3$ + 2* ⇌ *C*CH$_2$ + *H	100	30	$1.79 \times 10^{30\dagger}$	103
Surface_vdW_to_Bidentate					
4a	CHCH* + * ⇌ *CH*CH	—	−156	1.0×10^{21b}	—
4b	$CH_2CH_2^*$ + * ⇌ *CH$_2$*CH$_2$	11	−35	1.78×10^{21}	12
4c	CH$_2$O* + * ⇌ *CH$_2$*O	—	−44	1.0×10^{21b}	—
Surface_Adsorption_Bidentate					
5a	CHCH + 2* ⇌ *CH*CH	—	−255	0.83[¶c]	—
5b	CH$_2$CH$_2$ + 2* ⇌ *CH$_2$*CH$_2$	—	−148	0.69[¶c]	—
5c	CH$_2$O + 2* ⇌ *CH$_2$*O	—	−69	0.2[¶]	—
Surface_Monodentate_to_Bidentate					
6a	*CCH$_2$ + * ⇌ *C*CH$_2$	—	−148	1.0×10^{21b}	—
6b	*CHCH$_2$ + * ⇌ *CH*CH$_2$	3	−86	7.15×10^{20}	3
6c	H*CO + * ⇌ H*C*O	—	6	1.0×10^{21b}	—

[a] These reactions are endothermic in the reported direction. By default, all reactions are specified in the exothermic direction in RMG's generated mechanism. Therefore, the reverse direction was parameterized with an Arrhenius approach and provided as training data in RMG (see ESI). The forward direction was used to construct the BEP relation. [b] This is a guess, assuming transition state theory with $k_B T/h = 1 \times 10^{13}$ s^{-1}. [c] Literature values for the adsorption of acetylene are obtained from Vattuone *et al.*[42] and for ethylene from Brown *et al.*[43]

0 kJ mol^{-1} are used in the RMG database for training reactions 4a, 4c, 6a, and 6c. The rate of adsorption reactions, including bidentate adsorption, is described in RMG with a sticking coefficient S_0 in a modified Arrhenius-type equation

$$S_0 = A\left(\frac{T}{T_{ref}}\right)^{\beta} e^{\left(\frac{-E_a}{RT}\right)} \quad (3)$$

where A is dimensionless because it is a probability, and $T_{ref} = 1$ K. The calculated associative adsorption steps are barrierless, so fixed transition-state theory cannot be used, either. Instead, we use literature values for training reactions 5a and 5b. For the adsorption of acetylene (reaction 5a), a sticking coefficient of 0.83 is reported based on single-crystal adsorption calorimetry experiments on Pd.[42] An initial sticking coefficient of 0.69 is reported for the adsorption of ethylene on Pt(111).[43] Since no experimental data is available, we assume a sticking coefficient of 0.2 for the adsorption of formaldehyde.

RMG can estimate the reaction kinetics for elementary steps discovered by the templates of the reaction families from either a set of training reactions or hand-crafted BEP relations. The training reactions can be provided in (modified) Arrhenius form, whereas the BEP relations read as

$$E_a = E_a^0 + \alpha \Delta H_{rxn} \quad (4)$$

where E_a^0 is the intercept and α the slope, both obtained from linear regression to the DFT data. Training reactions and BEP rules are provided to give the user the freedom to choose between these estimation routines. Based on the results from

the transition state theory calculations and reaction enthalpies, we constructed BEP relations for the Surface_Bidentate_Dissociation, Surface_Dissociation, and Surface_Dissociation_to_Bidentate family. We considered the most stable final states for the calculation of the reaction enthalpy. The potential energy diagrams show that subsequent diffusion barriers leading to more stable final states are insignificant compared to the initial reaction barriers. Thence, once enough energy is present to cross the initial reaction barrier, the co-adsorbed system possesses enough energy to rearrange into a more stable final state. Using the most stable final state in the construction of the BEP relation is also consistent with the current assumption of no lateral interactions in RMG. Enthalpies of formation of the adsorbates that are present as reactant and product are obtained from the pre-compiled database or the estimation routine in the low-coverage limit at 1/9th ML. Therefore, the reaction enthalpy used to evaluate the BEP is in the low-coverage limit, too. A comparison of the enthalpies of formation obtained from DFT and the enthalpies of formation that RMG would predict based on current database values are provided in Table S3 in the ESI.† The BEP curves are shown in Fig. 2. All three reaction families have in common that the slope is close to 1, indicating rather late transition states with reaction coordinates close to the products.

Fig. S5† shows the rate constants calculated from DFT *versus* the rate constants calculated using a general rate rule in RMG, shown by eqn (4) in the ESI,† for the Surface_Bidentate_Dissociation, Surface_Dissociation, and Surface_Dissociation_to_Bidentate families.

Example: ethane dehydrogenation on Pt(111)

The new features added to RMG are used to generate a mechanism for the NDH of ethane on Pt(111) to produce ethylene. RMG's *core* was initialized with 5% C_2H_6 in N_2 with a vacant Pt(111) surface. This scenario is loosely based on the experiments of Riley *et al.*[28] who investigated Pt_xSn catalysts supported on Al_2O_3 for non-oxidative ethane dehydrogenation. The reader is referred to ref. 7, 8, 11 and 39 for details on the automated mechanism generation procedure with RMG and to ref. 13 for a detailed description of the workflow for heterogeneously catalyzed systems.

Mechanisms were generated using the ranged reactor feature in a temperature range of 623 to 973 K and a pressure of 1 bar. The maximum number of carbon atoms was set to 3 so as to expedite the mechanism generation process by avoiding larger species, and the maximum number of surface sites was set to 2 to focus on the bidentate chemistry. Gas-phase reactions were not considered, as they are not expected to be important around an operating temperature of 873 K (though RMG can simultaneously explore both gas and surface kinetics[12]). The mechanism expansion halts if the rate ratio (initial reaction rate divided by the rate of the expansion step) drops below a threshold of 10^{-7}. We determined this threshold through convergence tests, systematically varying it and monitoring both the mechanism size and predictions (see Fig. S7†), similar to the approach detailed in ref. 13. An acceptable value is identified when further reductions do not change the predictions of the microkinetic model. Larger thresholds lead to smaller mechanisms, and tighter thresholds enlarge the microkinetic model. Alternatively, a target conversion or simulation time can be used as a termination criterion.[7,8] However, these criteria may lead to extensive mechanisms if the reaction rates are slow, characteristic for a poorly performing catalyst. Further parameters for the mechanism generation are provided in Table 3. We rely solely on the general rate rules in the form of BEP relations instead of training reactions, since this approach has consistently led to excellent results in previous studies.[13,14,18]

Mechanisms were generated with and without the newly added bidentate reaction families for the ethane dehydrogenation over Pt(111) to demonstrate the impact of the new software features. Without the new bidentate functionalities, the microkinetic mechanism contains 22 species and 64 reactions. RMG still discovers C_2H_4 as well as CH_4, which demonstrates that there are both dehydrogenation and C–C cracking pathways involving only monodentate or physisorbed species. In contrast, when the new bidentate reaction families were included, the resulting microkinetic mechanism contains 52 species and 760 elementary steps. The size of the investigated

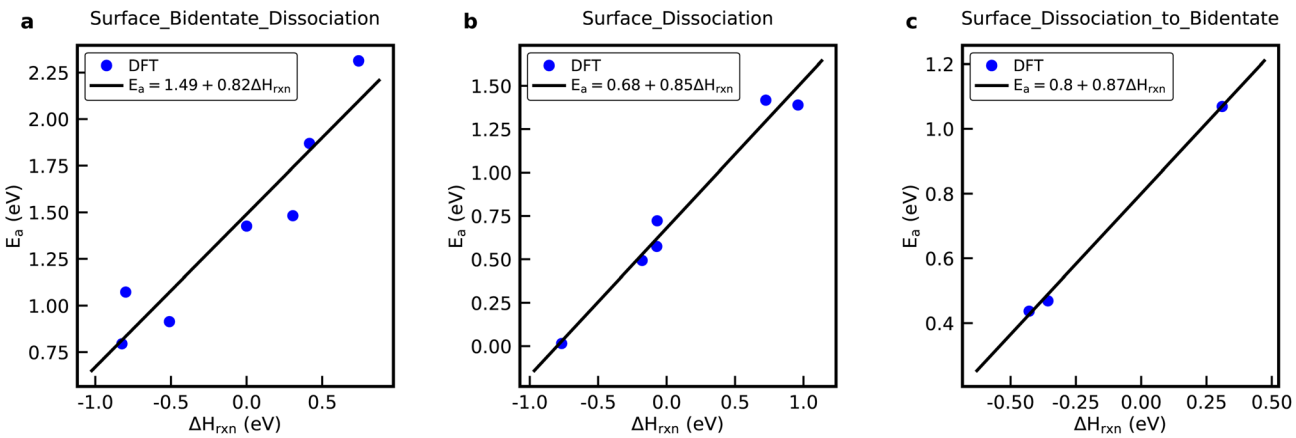

Fig. 2 DFT data and BEP relations for the (a) Surface_Bidentate_Dissociation, (b) Surface_Dissociation, and (c) Surface_Dissociation_to_Bidentate reaction family.

Table 3 RMG settings used for the mechanism generation procedure

Property	Value
Temperatures	623–973 K
nSim	7
Pressure	1 bar
Active site	Pt(111)
Surface site density	2.39×10^{-9} mol cm^{-2}
Specific surface area	1×10^{5} m^2 m^{-3}
toleranceMoveToCore, ε_{core}	1×10^{-1}
toleranceKeepInEdge, ε_{core}	1×10^{-8}
terminationRateRatio, ε_{rate}	1×10^{-7}
maximumCarbonAtoms	3
maximumSurfaceSites	2
maximumRadicalElectrons	0
Initial composition	5% C_2H_6, 95% N_2
Initial coverage	Vacant site fraction = 1.0

reaction space is also significantly expanded, as reflected in the size of the edge mechanism (see Table 4). Additionally, the time to generate the mechanism is increased by more than a factor of 10. Both C_2H_2 and C_3H_6 are additional discovered gas-phase species for the case with bidentate functionalities, and there are many adsorbates containing 3 carbon atoms (adsorbates with 4+ heavy atoms were restricted by design). In the mechanism generated with the bidentate reaction families, 17 bidentate adsorbates were discovered, and 52 reactions were direct hits from the newly added reaction families and rate rules. If a bidentate adsorbate is discovered, RMG will apply all existing reaction templates as it would do with monodentate species, leading to 594 reactions of the discovered mechanism ($\approx$80% of the reactions) involving bidentate adsorbates. These results highlight that the inclusion of bidentate functionalities leads to an exploration of a larger chemical reaction space. Therefore, the omission of bidentate reaction families neglects potentially kinetically relevant pathways.

Microkinetic modeling. Reactor simulations with the generated microkinetics models are performed with Cantera, an open-source software designed for detailed microkinetic simulations.[44] The simulated reactor is 25.4 cm long, with a 4 mm cross-section inner diameter, and an active Pt catalyst specific surface area of 4×10^3 m^{-1}, based on the experimental setup of Riley *et al.*[28] While the conditions are based on experimental studies, the intent is not to reproduce exactly the experimental results. Instead, the goal is to demonstrate the ability of RMG to discover all relevant pathways and produce reasonable results in realistic microkinetic simulations. The ethane dehydrogenation process was simulated as a plug-flow reactor using a chain of 100 continuously stirred tank reactors, assuming isothermal conditions. The feed (5% C_2H_6 and 95% N_2 molar composition) has an inlet velocity of 20 mL$_N$ min^{-1} and a temperature of 873 K at atmospheric pressure. In line with other studies in the literature, the simulation showed that ethylidyne (*CCH_3) is the most abundant surface intermediate during ethane dehydrogenation;[45] in fact, it covers up the entire Pt(111) surface (see Fig. S8†). However, *CCH_3 has repulsive lateral interactions, leading to a destabilization that prevents the formation of a complete monolayer. Therefore, we included a polynomial to describe the coverage-dependent enthalpy of formation (binding strength) based on DFT calculations (see ESI†). Only self-interactions were considered and all reported simulation results in the manuscript include the coverage dependence.

Fig. 3a shows the simulated gas-phase concentration profiles along the reactor length for the microkinetic model from the default RMG run and with the new bidentate features. Without any bidentate functionalities, RMG still discovers pathways leading to the formation of C_2H_4 and CH_4, but the overall activity of the catalyst is found to be extremely low. A C_2H_4 yield of 0.3% is obtained at the end of the reactor. The profiles change considerably when the new reaction families are included in the generation procedure. C_2H_4 and H_2 formation is dominating at the entrance of the reactor, while CH_4 formation *via* C–C cracking reactions gradually increases over the length of the reactor. At the end of the reactor, the C_2H_6 conversion reaches 14.3% with a selectivity towards C_2H_4 of 56.4%. Additionally, the formation of traces of C_2H_2 and C_3H_6 is predicted, which is also observed experimentally for Pt-containing catalysts.[28]

Surface coverages play a significant role in the dominating pathways and influence the composition of the product stream. Interestingly, the new reaction families do not change the coverage profiles (see Fig. 3b). The surface is mostly covered by (*CCH_3), which is the most stable adsorbate, with the lowest free energy of formation (Fig. 4), methylidyne (*CH), and surface carbon (*C). This observation can be attributed to the fact that no bidentate species are involved in the formation of *CCH_3 (see below). However, bidentate pathways are required to crack or dehydrogenate *CCH_3 further. Yet, with bidentate features, new pathways were discovered that lead to deeply dehydrogenated species with 3 carbon atoms, such as *C*CCH_3 and *CH*CCH_2. These species are considered to be precursors for coke formation, a major challenge during NDH of ethane and propane.[24,46,47] Without a truncation of the maximum chain length size, it would have been possible for RMG to discover

Table 4 Results from the mechanism generation with the new reaction families

	Without bidentate reaction families	With bidentate reaction families
Core	22 species/64 reactions	52 species/760 reactions
Edge	19 species/38 reactions	19 species/434 reactions
Generation time[a]	01:42 min	16:46 min

[a] Mechanisms were generated with a single core of an Intel Core i7-8565U CPU.

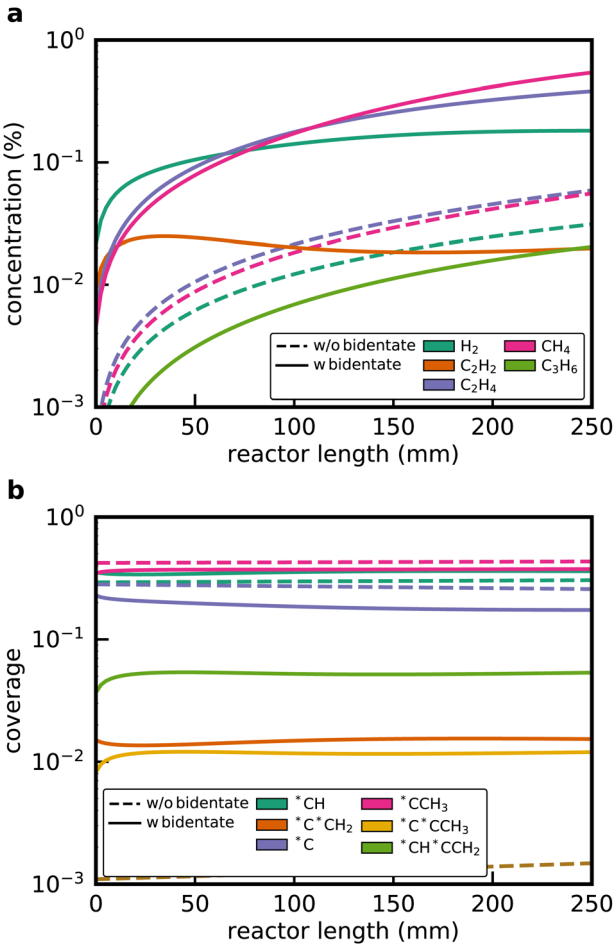

Fig. 3 (a) Gas-phase concentration and (b) coverage profiles for the non-oxidative ethane dehydrogenation over Pt(111) along the 1D packed bed reactor. Simulations are performed for the case without bidentate functionalities and with the new reaction families.

even larger precursors for coke formation, thereby further expanding the considered reaction space.

Reaction mechanism. Reaction path analysis was conducted at the initial conditions of the reactor using Cantera's reaction path analyzer, illustrated in Fig. S9.† A potential energy diagram that compares the main ethylene formation pathways comparing the two RMG cases is displayed in Fig. 4. The reaction pathways for the activation of C_2H_6 generated without bidentate functionalities and with the new features are identical. First, C_2H_6(g) adsorbs dissociatively to form adsorbed ethyl ($*CH_2CH_3$) and a hydrogen adatom (H*). An H-abstraction reaction removes one of the α-H in ethyl to form $*CHCH_3$. $*CCH_3$ is then formed *via* another H abstraction by surface carbon, C*. Following the pathways with only monodentate species, *C abstracts a H from $*CCH_3$ to produce monodentate $*CCH_2$ and the carbon atom is subsequently hydrogenated to physisorbed $C_2H_4^*$.

With bidentate features, the dissociation of the C–H bond in $*CCH_3$ leads to the formation of $*C*CH_2$, as discovered by the Surface_Dissociation_to_Bidentate family, which is considerably more stable than the monodentate counterpart ($\Delta E_b = 1.3$ eV) (see Fig. 4). Additionally, the barriers for the monodentate pathway are considerably higher, which explains the low reactivity seen in Fig. 3. This bidentate species is then hydrogenated to C_2H_4 *via* bidentate vinyl ($*CH*CH_2$) and di-σ ethylene ($*CH_2*CH_2$). Formation of acetylene occurs if the $*C*CH_2$ is further dehydrogenated to *C*CH, followed by hydrogenation of the carbon atom.

All intermediates and pathways discussed in the literature were successfully discovered by RMG.[25,45] Yet, the main pathways for C_2H_4 formation uncovered in the reaction path analysis are in disagreement with the proposed path in the literature. Hansen *et al.*[25] showed that $*CH_2CH_3$ is directly dehydrogenated to a physisorbed $CH_2CH_2^*$, following the proposed Horiuti–Polanyi mechanism.[48] RMG discovered this elementary step and a similar elementary step, where a bidentate $*CH_2$-$*CH_2$ is formed instead of the physisorbed species. As shown in Fig. 4, the reaction pathway with the physisorbed species has a large activation barrier compared to a relatively low activation barrier for the one-step formation of $*CH_2*CH_2$. It is debatable whether the assumption of physisorbed ethylene by Hansen *et al.*[25] is justified, as the relaxed geometry clearly shows a bidentate species, which is usually more stable. The transition state calculation showed that bidentate $*CH_2*CH_2$ is stabilized by 0.4 eV and there is only a small barrier connecting the physisorbed and bidentate well, which makes it meta-stable, especially if the entropy increases at high temperatures. This fact might seem not relevant at first, but it has an impact on the reaction order, which changes from a first-order reaction with respect to vacant sites ($*CH_2CH_3 + * \rightleftharpoons CH_2CH_2^* + *H$) to a second-order reaction ($*CH_2CH_3 + 2* \rightleftharpoons *CH_2*CH_2 + *H$). The second-order reaction is orders of magnitude slower for the same amount of available vacant sites. Therefore, this pathway is too slow to occur on the highly covered Pt(111) surface in the generated microkinetic model.

Admittedly, our treatment of coverage dependence for this intricate system is rather simplistic. A completely covered Pt surface is not possible since all these species exhibit strong repulsive interactions. For a more rigorous description, it would be necessary to subject all adsorbates that have a high coverage with lateral interactions as well as cross interactions, but that is beyond the scope of the present work.

Interestingly, most of the hydrogenation or dehydrogenation steps of the adsorbates occur through abstraction (or bimolecular-to-bimolecular) reactions by *C or *CH, respectively. Given the high coverages of these adsorbates, the pathways are actually reasonable and consistent within this study, albeit in disagreement with the literature. Abstraction reactions are often not considered in the literature for heterogeneously catalyzed reactions. Yet, abstraction reactions make up a significant portion of elementary steps in gas-phase reaction mechanisms. One notable exception are oxidative dehydrogenation steps during oxidation of, *e.g.*, ethane.[49] However, the abstraction to C and larger moieties is often not considered. This omission has multiple reasons, such as the increasing complexity of potential configuration on a facet as well as the increasing computational costs. Additionally, including all possible bimolecular reactions results in a combinatorial

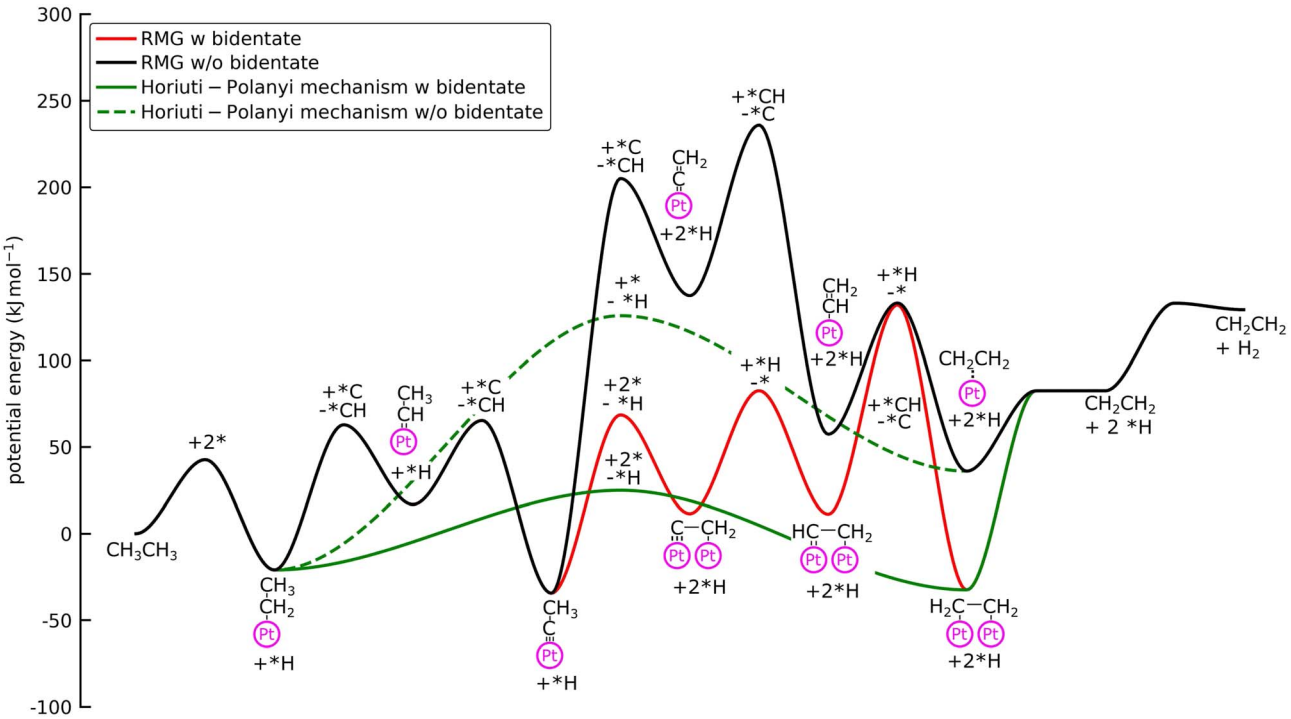

Fig. 4 Potential energy diagram of the main pathway for the NDH of C_2H_6 on Pt(111) generated with RMG with bidentate features and without bidentate features. The green line shows the Horiuti–Polanyi mechanism, where adsorbed propyl ($*CH_2CH_3$) is directly dehydrogenated to bidentate ethylene ($*CH_2*CH_2$). *H is omitted for clarity and the spectator species *C and *CH are not considered in the calculation of the enthalpy. Barrier heights are activation energies and not the energies of the first-order saddle points. The species on the activation barrier is the co-reactant for the abstraction reaction indicated with a '+' for the forward reaction and '−' for the backward reaction.

explosion of possible pathways.[50] These facts contribute to the omission of these pathways and the dominance of dissociation reactions in the literature. We are currently in the process of improving the rate rules to provide better estimates for these reactions so that it is possible to elucidate the importance of these reactions with a higher certainty. It has also to be mentioned that the catalysts consists of a range of different facets, which can all contribute to the activity.[47] This complex morphology has to be considered during the mechanism generation and multiscale modeling for a fair comparison with experiments.[2,51]

Ultimately, our goal with this study is not to provide conclusive new insights into the ethane dehydrogenation chemistry but to demonstrate that RMG can generate plausible mechanisms for systems involving bidentate species. With the newly added bidentate features, RMG discovers a mechanism that contains all the relevant intermediates and pathways that are discussed in the literature for the NDH of C_2H_6.[25] The usage of RMG to generate a mechanism is just a starting point in the mechanism exploration. A better agreement can be achieved *via* iterative refinement of the most important energetic parameters identified by degree of rate control analysis[13] or *via* rigorous uncertainty quantification in all possible parameters.[14,18] The big advantage of RMG is the exhaustive exploration of all possible reactions. Thus, the software can uncover new pathways that are worth investigating with DFT calculations, *e.g.* the abstraction reactions.

Automated mechanism generation with linear scaling

RMG can utilize linear scaling relations to scan the periodic table to reveal more active or selective materials.[15] In the prior literature, when looking for an improved catalyst *via* linear scaling relations, a static mechanism with a fixed rate-determining step is often assumed.[25,52–54] In contrast, RMG generates a new mechanism for every point in the descriptor space and does not rely on these simplifying assumptions. Thus, RMG can capture changes in the mechanism since only the kinetically relevant pathways are included due to the objective selection by the rate-based algorithm. To demonstrate RMG's ability to apply scaling relations for mechanisms involving bidentate adsorbates, we screened for improved dehydrogenation catalysts by considering other close-packed monometallic facets and bimetallic alloys. The selection of the catalyst in RMG is performed by either selecting metals from a pre-compiled database or by providing binding energies for the descriptor species, in this case, *C and *H. The binding energies for the monometallic facets are provided in RMG's database and can be called *via* the metal property tag. We confirmed that the linear scaling relations implemented in RMG are suitable to accurately determine the heats of formation of the bidentate species when scaling from a Pt(111) database, which is discussed in the ESI.†

Fig. 5 shows the results from the mechanism generation for the monometallic close-packed surfaces. Every generated mechanism is unique and has its own set of elementary steps

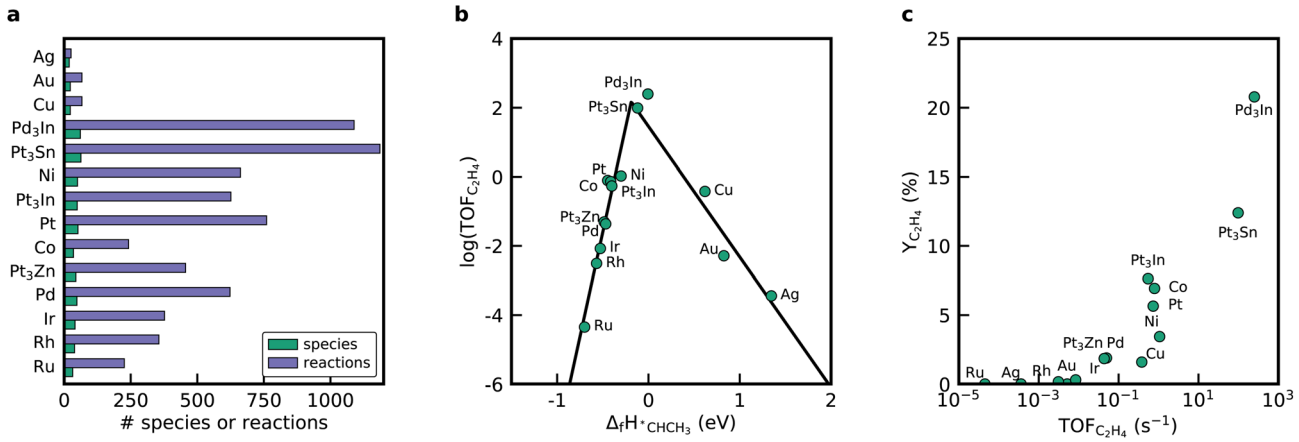

Fig. 5 (a) Metrics of the mechanism generation sorted according to the carbon binding energy going from weakest (Ag) to strongest (Ru). (b) Volcano diagram of the ethylene production turnover frequency at 873 K, $p_{C_2H_6} = 0.05$ bar, and $p_{N_2} = 0.95$ bar. (c) End-of-pipe ethylene yield as a function of the turnover frequency of C_2H_6 to C_2H_4 at 873 K.

and intermediates, which is easily seen by looking at the mechanism metrics in Fig. 5a. Among the tested metals, noble metals like Ag, Cu, and Au have only very small mechanisms, whereas the largest reaction mechanisms were discovered for Pt, Ni, and Co. The time it takes to generate the mechanisms also varies significantly across the different metals. Reactor simulations conducted with the microkinetic models for all metals show only meager C_2H_6 conversion rates for Ag, Au, and Cu (see ESI†), which is why the mechanism expansion stops early. If the initial production rate is fast due to the adsorption of gas molecules on the surface, but the following reactions on the surface are slow, the threshold for the termination criterion (*i.e.* the rate ratio), will be reached quickly.

Fig. 5b shows a volcano diagram with the turnover frequency (TOF) for the ethylene production at the initial conditions of the reactor. As a simplification for the linear screening study, we assumed that the coverage dependence of $*CCH_3$ is identical on all close-packed metal surfaces. Concentration profiles in the reactor are provided in Fig. S12.† Mapping the TOF as a function of the enthalpy of formation of $*CHCH_3$ results in a volcano curve based on the monometallic facets. $*CHCH_3$ is identified in the literature to be the selectivity and activity descriptor for NDH.[25] The noble metals are located on the right-hand side of the volcano curve, binding $*CHCH_3$ weakly. The rest of the metals are on the left-hand side and exhibit a strong binding energy for $*CHCH_3$. Overall, the activity for ethylene formation at the inlet conditions of the reactor increases in the order Ru < Ag < Au < Rh < Ir < Pd < Cu < Co < Pt < Ni, which is in agreement with literature studies for these close-packed facets. The selectivity towards ethylene obtained at the end of the reactor is highest for Pt(111) and Co(0001).

To enhance the activity and selectivity of the catalyst for the NDH, alloying Pt and Pd with other transition metals is a common approach. In the literature, it was identified that Pt_3Sn, Pt_3Zn, Pt_3In, and Pd_3In are promising candidates.[19] Accordingly, we generated mechanisms for these alloys using binding energies for *C and *H for the bimetallic catalysts derived from structures from Catalysis-Hub[55] (see ESI†), which are based on the work of Hansen *et al.*[25] These bimetallic catalysts align nicely onto the volcano curve created from the monometallic surface. The highest activity is obtained for the $Pd_3In(111)$ surface, followed by $Pt_3Sn(111)$. Both catalysts also show the highest C_2H_4 yields at the end of the reactor (see Fig. 5). Next to C_2H_4 and C_2H_2, RMG predicts that these catalysts also form propylene, propyne (CH_3CCH) and allene (CH_2CCH_2). Riley *et al.*[28] observed traces of propylene, supporting the results from the automatically generated mechanisms. Co(111) and Ni(111) also form small amounts of C_3H_6 (see Fig. S12†).

Degree of rate control (DRC) analysis was performed to determine the rate-controlling steps and intermediates.[56,57] The elementary steps with the highest DRC for every catalyst are shown in Fig. 6a. Dissociation of $*CH_2CH_3$ to $*CHCH_3$ is the elementary step with the highest DRC for the noble metals Au and Ag. The rate-controlling step of the Horiuti–Polanyi mechanism is the dehydrogenation of ethyl to ethylene ($*CH_2CH_3 + 2* \rightleftharpoons *CH_2*CH_2 + *H$), which is also obtained for Cu, Pt, Ni, Pt_3Sn, and Pd_3In. Dissociative adsorption of ethane is rate-limiting for the metals that bind carbon strongly. Interestingly, the production rate of C_2H_4 is reduced when the dissociative adsorption rate of H_2 is increased on Pt_3In, Pd and Co. However, for the other metals, a high positive DRC is observed for this reaction, which shows that increasing the adsorption rate of H_2 can potentially increase the C_2H_4 formation rate. Therefore, co-feeding H_2 during NDH can be used to accelerate ethane conversion and increase the selectivity towards C_2H_4.[25,46] Similar results are obtained for the thermodynamic degree of rate control (TDRC) as seen in Fig. 6b. Adsorbates with a high thermodynamic degree of rate control are *C, *CH, and $*CCH_3$. These species have a high coverage on the surface and participate in many of the abstraction reactions that lead to $*CH_2$-$*CH_2$. Our result shows that it is not justified to assume a fixed rate-determining elementary step or rate-controlling intermediate when changing the binding strength of carbon by multiple eV to scale across the periodic table. A similar

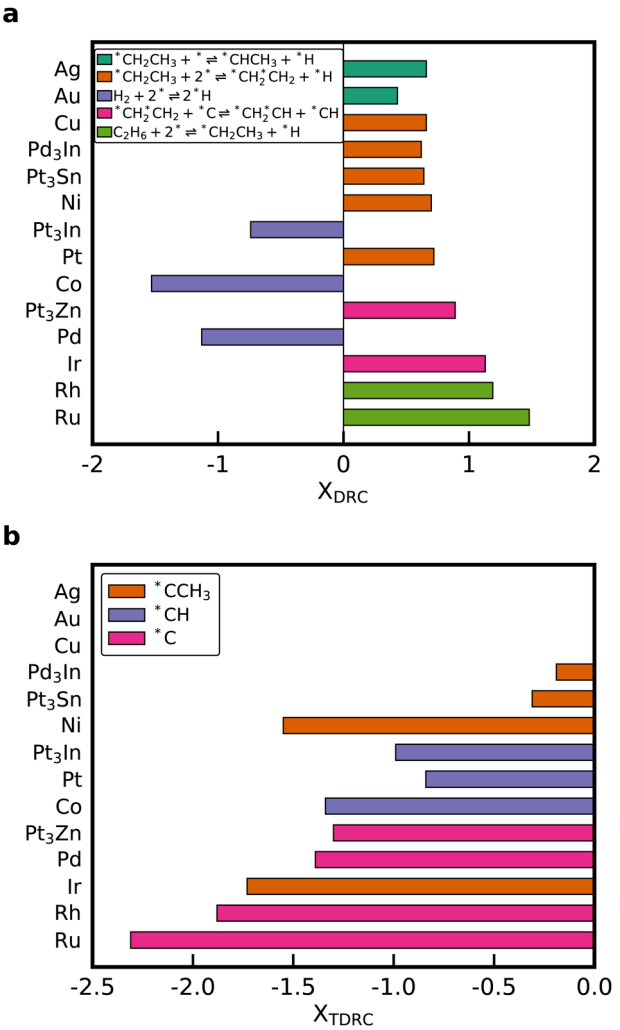

Fig. 6 (a) Elementary reaction with the highest degree of rate control X_{DRC} and (b) adsorbate with the highest thermodynamic degree of rate control X_{TDRC} for each metal. Metals are sorted according to the carbon binding energy going from weakest (Ag) to strongest (Ru). There is no species with a significant TDRC for Ag, Au, Cu, because the surface is vacant under the operating conditions.

variability in the DRC was observed when perturbing the parameters of a microkinetic model within their correlated uncertainty space.[14,18]

Future development directions. Including bidentate functionalities into RMG is a significant step towards the automated exploration of the chemistry of larger molecules. Our study and previous work show that RMG works well for close-packed metal facets, especially for the (111) termination, since well-populated databases are available.[12,14,17,18] Larger multidentate adsorbates are crucial in modeling coke formation on the catalyst and deactivation, which is a common nuisance in many conversion reactions of hydrocarbons. Capturing the coking of the catalyst requires new reaction templates and estimation routines that enable the formation of cyclic adsorbates. Polycyclic aromatic hydrocarbons such as naphthalene ($C_{10}H_8$) or acenaphthylene ($C_{12}H_8$) are often reported as gas-phase precursors for coke formation.[58,59] This study serves as a blueprint, outlining the steps necessary to extend RMG towards these larger (cyclic) multidentate species or to add other functionalities. Furthermore, we are currently working on including coverage dependence on energetic parameters and multiple surface sites in the generation procedure to achieve a more realistic description of the multifaceted catalyst under working conditions. A long-term objective is the inclusion of functionalities for metal oxide catalysis into RMG to enable the consideration of the catalyst support in the mechanism generation procedure.

Conclusions

We have enhanced the capabilities of the open-source software RMG for heterogeneously catalyzed reactions to cope with the complexity of multidentate adsorbates. New reaction families were added and generalized rate rules were parameterized with *ab initio* calculations. RMG was applied in a test case to automatically generate mechanisms for the non-oxidative dehydrogenation of C_2H_6 on Pt(111), an essential process for the formation of ethylene. A reaction mechanism that consisted of around 90% of elementary reactions involving bidentate species was discovered. Although the considered intermediates and species agree with the literature, the dominant pathway at the investigated temperature proceeds primarily *via* abstraction reactions pointing to further development directions for the catalysis branch of RMG. In conclusion, with the significant updates performed in this work, RMG can now explore reaction mechanisms for processes involving larger adsorbates.

Data availability

The raw DFT data, the RMG database used for the mechanism generation, the generated mechanisms, all scripts used for the simulation and analysis in this paper as well as the scripts used to make the figures are available at **https://zenodo.org/record/8341630** with DOI: **https://doi.org/10.5281/zenodo.8341630**.

Conflicts of interest

There are no conflicts of interest to declare.

Acknowledgements

The authors thank Chris Blais and Chao Xu for helpful suggestions. BK, KB and CFG gratefully acknowledge support by the U.S. Department of Energy, Office of Science, Basic Energy Sciences, under Award #0000232253 and #DE-SC0019441, as part of the Computational Chemical Sciences Program. BK acknowledges financial support from the Alexander von Humboldt Foundation. This research used resources of the Argonne Leadership Computing Facility, which is a DOE Office of Science User Facility supported under Contract DE-AC02-06CH11357.

References

1 A. Bruix, J. T. Margraf, M. Andersen and K. Reuter, First-Principles-Based Multiscale Modelling of Heterogeneous Catalysis, *Nat. Catal.*, 2019, **2**, 659–670.
2 G. D. Wehinger, *et al.*, Quo Vadis Multiscale Modeling in Reaction Engineering? – A Perspective, *Chem. Eng. Res. Des.*, 2022, **184**, 39–58.
3 B. Zijlstra, R. J. P. Broos, W. Chen, G. L. Bezemer, I. A. W. Filot and E. J. M. Hensen, The Vital Role of Step-Edge Sites for Both CO Activation and Chain Growth on Cobalt Fischer–Tropsch Catalysts Revealed through First-Principles-Based Microkinetic Modeling Including Lateral Interactions, *ACS Catal.*, 2020, **10**, 9376–9400.
4 S. Vernuccio and L. J. Broadbelt, Discerning Complex Reaction Networks Using Automated Generators, *AIChE J.*, 2019, **65**, e16663.
5 S. Rangarajan, A. Bhan and P. Daoutidis, Language-Oriented Rule-Based Reaction Network Generation and Analysis: Description of RING, *Comput. Chem. Eng.*, 2012, **45**, 114–123.
6 S. Rangarajan, R. R. O. Brydon, A. Bhan and P. Daoutidis, Automated Identification of Energetically Feasible Mechanisms of Complex Reaction Networks in Heterogeneous Catalysis: Application to Glycerol Conversion on Transition Metals, *Green Chem.*, 2014, **16**, 813–823.
7 C. W. Gao, J. W. Allen, W. H. Green and R. H. West, Reaction Mechanism Generator: Automatic Construction of Chemical Kinetic Mechanisms, *Comput. Phys. Commun.*, 2016, **203**, 212–225.
8 M. Liu, A. G. Dana, M. Johnson, M. Goldman, A. Jocher, A. M. Payne, C. Grambow, K. Han, N. W.-W. Yee, E. Mazeau, K. Blöndal, R. West, F. Goldsmith and W. H. Green, Reaction Mechanism Generator v3.0: Advances in Automatic Mechanism Generation, *J. Chem. Inf. Model.*, 2021, **61**, 2686–2696.
9 W. H. Green and R. H. West, *RMG – Reaction Mechanism Generator Version 3.0*, 2023, **https://rmg.mit.edu/**, accessed 2023-02-16.
10 F. H. Vermeire, S. U. Aravindakshan, A. Jocher, M. Liu, T.-C. Chu, R. E. Hawtof, R. Van de Vijver, M. B. Prendergast, K. M. Van Geem and W. H. Green, Detailed Kinetic Modeling for the Pyrolysis of a Jet A Surrogate, *Energy Fuels*, 2022, **36**, 1304–1315.
11 C. F. Goldsmith and R. West, Automatic Generation of Microkinetic Mechanisms in Heterogeneous Catalysis, *J. Phys. Chem. C*, 2017, **121**, 9970–9981.
12 K. Blöndal, J. Jelic, E. Mazeau, F. Studt, R. H. West and C. F. Goldsmith, Computer-Generated Kinetics for Coupled Heterogeneous/Homogeneous Systems: A Case Study in Catalytic Combustion of Methane on Platinum, *Ind. Eng. Chem. Res.*, 2019, **58**, 17682–17691.
13 B. Kreitz, P. Lott, J. Bae, K. Blöndal, S. Angeli, Z. W. Ulissi, F. Studt, C. F. Goldsmith and O. Deutschmann, Detailed Microkinetics for the Oxidation of Exhaust Gas Emissions through Automated Mechanism Generation, *ACS Catal.*, 2022, **12**, 11137–11151.
14 B. Kreitz, K. Sargsyan, E. J. Mazeau, K. Blöndal, R. H. West, G. D. Wehinger, T. Turek and C. F. Goldsmith, Quantifying the Impact of Parametric Uncertainty on Automatic Mechanism Generation for CO_2 Hydrogenation on Ni(111), *JACS Au*, 2021, **1**, 1656–1673.
15 E. Mazeau, P. Satpute, K. Blöndal, F. Goldsmith and R. West, Automated Mechanism Generation Using Linear Scaling Relationships and Sensitivity Analyses Applied to Catalytic Partial Oxidation of Methane, *ACS Catal.*, 2021, **11**, 7114–7125.
16 B. Kreitz, G. D. Wehinger, C. F. Goldsmith and T. Turek, in *30th European Symposium on Computer Aided Process Engineering*, ed. Pierucci, S., Manenti, F., Bozzano, G. L. and Manca, D., Comput.-Aided Chem. Eng., Elsevier, 2020, vol. 48, pp. 529–534.
17 B. Kreitz, G. D. Wehinger, C. F. Goldsmith and T. Turek, Microkinetic Modeling of the Transient CO_2 Methanation with DFT-Based Uncertainties in a Berty Reactor, *ChemCatChem*, 2022, e202200570.
18 B. Kreitz, P. Lott, F. Studt, A. J. Medford, O. Deutschmann and C. F. Goldsmith, Automated Generation of Microkinetics for Heterogeneously Catalyzed Reactions Considering Correlated Uncertainties, *Angew. Chem., Int. Ed.*, 2023, e202306514.
19 J. J. H. B. Sattler, J. Ruiz-Martinez, E. Santillan-Jimenez and B. M. Weckhuysen, Catalytic Dehydrogenation of Light Alkanes on Metals and Metal Oxides, *Chem. Rev.*, 2014, **114**, 10613–10653.
20 L. M. Madeira and M. F. Portela, Catalytic oxidative dehydrogenation of n-butane, *Catal. Rev.*, 2002, **44**, 247–286.
21 H. Saito and Y. Sekine, Catalytic Conversion of Ethane to Valuable Products through Non-Oxidative Dehydrogenation and Dehydroaromatization, *RSC Adv.*, 2020, **10**, 21427–21453.
22 D. Fairuzov, I. Gerzeliev, A. Maximov and E. Naranov, Catalytic Dehydrogenation of Ethane: A Mini Review of Recent Advances and Perspective of Chemical Looping Technology, *Catalysts*, 2021, **11**, 833.
23 C. Samanta and R. K. Das, in *Catalysis for Clean Energy and Environmental Sustainability: Petrochemicals and Refining Processes – Volume 2*, ed. Pant, K. K., Gupta, S. K. and Ahmad, E., Springer International Publishing, Cham, 2021, pp. 149–204.
24 M. Huš, D. Kopač and B. Likozar, Kinetics of Non-Oxidative Propane Dehydrogenation on Cr2O3 and the Nature of Catalyst Deactivation from First-Principles Simulations, *J. Catal.*, 2020, **386**, 126–138.
25 M. H. Hansen, J. K. Nørskov and T. Bligaard, First Principles Micro-Kinetic Model of Catalytic Non-Oxidative Dehydrogenation of Ethane over Close-Packed Metallic Facets, *J. Catal.*, 2019, **374**, 161–170.
26 V. Galvita, G. Siddiqi, P. Sun and A. T. Bell, Ethane dehydrogenation on Pt/Mg(Al)O and PtSn/Mg(Al)O catalysts, *J. Catal.*, 2010, **271**, 209–219.

27 S. Liu, B. Zhang and G. Liu, Metal-Based Catalysts for the Non-Oxidative Dehydrogenation of Light Alkanes to Light Olefins, *React. Chem. Eng.*, 2021, **6**, 9–26.
28 C. R. Riley, A. De La Riva, I. L. Ibarra, A. K. Datye and S. S. Chou, Achieving High Ethylene Yield in Non-Oxidative Ethane Dehydrogenation, *Appl. Catal., A*, 2021, **624**, 118309.
29 P. Giannozzi, *et al.*, Quantum ESPRESSO: a modular and open-source software project for quantum simulations of materials, *J. Phys.: Condens. Matter*, 2009, **21**, 395502.
30 P. Giannozzi, *et al.*, Advanced capabilities for materials modelling with Quantum ESPRESSO, *J. Phys.: Condens. Matter*, 2017, **29**, 465901.
31 K. Berland and P. Hyldgaard, Exchange functional that tests the robustness of the plasmon description of the van der Waals density functional, *Phys. Rev. B: Condens. Matter Mater. Phys.*, 2014, **89**, 035412.
32 K. Berland, C. A. Arter, V. R. Cooper, K. Lee, B. I. Lundqvist, E. Schröder, T. Tronhauser and P. Hyldgaard, van der Waals density functionals built upon the electron-gas tradition: facing the challenge of competing interactions, *J. Chem. Phys.*, 2014, **140**, A539.
33 D. R. Hamann, Optimized norm-conserving Vanderbilt pseudopotentials, *Phys. Rev. B: Condens. Matter Mater. Phys.*, 2013, **88**, 085117.
34 M. Schlipf and F. Gygi, Optimization algorithm for the generation of ONCV pseudopotentials, *Comput. Phys. Commun.*, 2015, **196**, 36–44.
35 N. Marzari, D. Vanderbilt, A. De Vita and M. C. Payne, Thermal Contraction and Disordering of the Al(110) Surface, *Phys. Rev. Lett.*, 1999, **82**, 3296.
36 S. R. Bahn and K. W. Jacobsen, An object-oriented scripting interface to a legacy electronic structure code, *Comput. Chem. Eng.*, 2002, **4**, 56–66.
37 E. D. Hermes, K. Sargsyan, H. N. Najm and J. Zádor, Accelerated Saddle Point Refinement through Full Exploitation of Partial Hessian Diagonalization, *J. Chem. Theory Comput.*, 2019, **15**, 6536–6549.
38 J. Bae, C. F. Goldsmith and A. A. Peterson, 2023, in preparation.
39 M. S. Johnson, *et al.*, RMG Database for Chemical Property Prediction, *J. Chem. Inf. Model.*, 2022, **62**, 4906–4915.
40 C. F. Goldsmith, Estimating the Thermochemistry of Adsorbates Based Upon Gas-Phase Properties, *Top. Catal.*, 2012, **55**, 366–375.
41 B. Kreitz, K. Blöndal, K. Badger, R. H. West and C. F. Goldsmith, *Data for Automatic Mechanism Generation Involving Kinetics of Surface Reactions with Bidentate Adsorbates*, 2023, DOI: **10.5281/zenodo.8341630**.
42 L. Vattuone, Y. Y. Yeo, R. Kose and D. A. King, Energetics and kinetics of the interaction of acetylene and ethylene with Pd100 and Ni100, *Surf. Sci.*, 2000, **447**, 1–14.
43 W. A. Brown, R. Kose and D. A. King, Femtomole Adsorption Calorimetry on Single-Crystal Surfaces, *Chem. Rev.*, 1998, **98**, 797–832.
44 D. G. Goodwin, H. K. Moffat, I. Schoegl, R. L. Speth and B. W. Weber, *Cantera: An Object-oriented Software Toolkit for Chemical Kinetics, Thermodynamics, and Transport Processes*, 2022, **https://www.cantera.org**, Version 2.6.0.
45 L. Skubic, J. Sovdat, N. Teran, M. Huš, D. Kopač and B. Likozar, Ab Initio Multiscale Process Modeling of Ethane, Propane and Butane Dehydrogenation Reactions: A Review, *Catalysts*, 2020, **10**, 1405.
46 S. Saerens, M. K. Sabbe, V. V. Galvita, E. A. Redekop, M.-F. Reyniers and G. B. Marin, The Positive Role of Hydrogen on the Dehydrogenation of Propane on Pt(111), *ACS Catal.*, 2017, **7**, 7495–7508.
47 C. Fricke, B. Rajbanshi, E. A. Walker, G. Terejanu and A. Heyden, Propane Dehydrogenation on Platinum Catalysts: Identifying the Active Sites through Bayesian Analysis, *ACS Catal.*, 2022, **12**, 2487–2498.
48 I. Horiuti and M. Polanyi, Exchange Reactions of Hydrogen on Metallic Catalysts, *Trans. Faraday Soc.*, 1934, **30**, 1164.
49 N. R. Peela, J. E. Sutton, I. C. Lee and D. G. Vlachos, Microkinetic Modeling of Ethane Total Oxidation on Pt, *Ind. Eng. Chem. Res.*, 2014, **53**, 10051–10058.
50 J. T. Margraf and K. Reuter, Systematic Enumeration of Elementary Reaction Steps in Surface Catalysis, *ACS Omega*, 2019, **4**, 3370–3379.
51 B. Kreitz, G. D. Wehinger, C. F. Goldsmith and T. Turek, Microkinetic Modeling of the CO_2 Desorption from Supported Multifaceted Ni Catalysts, *J. Phys. Chem. C*, 2021, **125**, 2984–3000.
52 A. J. Medford, A. C. Lausche, F. Abild-Pedersen, B. Temel, N. C. Schjødt, J. K. Nørskov and F. Studt, Activity and Selectivity Trends in Synthesis Gas Conversion to Higher Alcohols, *Top. Catal.*, 2014, **57**, 135–142.
53 G. Jones, F. Studt, F. Abild-Pedersen, J. K. Nørskov and T. Bligaard, Scaling Relationships for Adsorption Energies of C2 Hydrocarbons on Transition Metal Surfaces, *Chem. Eng. Sci.*, 2011, **66**, 6318–6323.
54 C. A. Wolcott, A. J. Medford, F. Studt and C. T. Campbell, Degree of Rate Control Approach to Computational Catalyst Screening, *J. Catal.*, 2015, **330**, 197–207.
55 K. T. Winther, M. J. Hoffmann, J. R. Boes, O. Mamun, M. Bajdich and T. Bligaard, Catalysis-Hub.Org, an Open Electronic Structure Database for Surface Reactions, *Sci. Data*, 2019, **6**, 75.
56 C. T. Campbell, Finding the Rate-Determining Step in a Mechanism, *J. Catal.*, 2001, **204**, 520–524.
57 C. T. Campbell, The Degree of Rate Control: A Powerful Tool for Catalysis Research, *ACS Catal.*, 2017, **7**, 2770–2779.
58 T.-C. Chu, Z. J. Buras, P. Oßwald, M. Liu, M. J. Goldman and W. H. Green, Modeling of aromatics formation in fuel-rich methane oxy-combustion with an automatically generated pressure-dependent mechanism, *Phys. Chem. Chem. Phys.*, 2019, **21**, 813–832.
59 J. Bae, J. Hashemi, D. Yun, D. K. Kim, D. H. Choo, C. F. Goldsmith and A. A. Peterson, Non-oxidative methane conversion by Fe single site catalysts: quantifying temperature limitations imposed by gas-phase pyrolysis, *Catal. Sci. Technol.*, 2022, **12**, 6903–6919.